

Experimental fault-tolerant code switching

Received: 11 July 2024

Accepted: 1 November 2024

Published online: 24 January 2025



Check for updates

Ivan Pogorelov  ^{1,5}, Friederike Butt  ^{2,3,5}, Lukas Postler¹, Christian D. Marcinia  ¹, Philipp Schindler  ¹, Markus Müller  ^{2,3} & Thomas Monz ^{1,4}

Quantum error correction is essential for mitigating hardware errors in quantum computers by encoding logical information into several physical qubits. However, no single error-correcting code intrinsically supports a fault-tolerant implementation of all the gates needed for universal quantum computing. One approach for addressing this problem is to switch between two suitable error-correcting codes that in combination provide a fault-tolerant universal gate set. Here we present the experimental implementation of fault-tolerant code switching between two different codes in a trapped-ion processor. We switch between the 7-qubit colour code, which features fault-tolerant CNOT and H quantum gates, and the 10-qubit code, which allows for a fault-tolerant T gate implementation. Together, these codes form a complementary universal gate set. We construct logical circuits and prepare 12 different logical states that are not accessible natively in a fault-tolerant way within a single code. Finally, we use code switching to entangle two logical qubits using the full universal gate set in a single logical quantum circuit. Our results experimentally demonstrate a route towards deterministic control over logical qubits with low auxiliary qubit overhead and without relying on the probabilistic preparation of resource states.

Quantum computers offer the prospect of performing certain computational tasks more efficiently than any known classical algorithm^{1,2}. However, the accuracy of quantum computations is limited by noise arising from the interaction of qubits with their environment and imperfect control operations³. Quantum error correction (QEC) addresses this challenge by encoding quantum information across several physical qubits, thereby adding redundancy and allowing errors to be localized and corrected without destroying the encoded information^{4,5}. QEC is performed by physical operations that are themselves faulty. Operations on these error-corrected logical qubits, therefore, must be performed without proliferating local errors uncontrollably across the encoded qubit. This can be achieved with fault-tolerant (FT) circuit designs⁶⁻⁹, for example, by using very resource-efficient transversal gates. Transversal gate operations perform logical operations by qubit-wise application of (not necessarily identical) physical operations.

Generally, it is not possible to implement an arbitrary logical operation transversally on a given QEC code. Computations on qubits can be approximated to arbitrary precision using only a finite set of gates that form a so-called universal gate set^{5,10}. For example, a gate set consisting of a Hadamard gate (H), a T gate and a 2-qubit-entangling controlled NOT (CNOT) gate would allow for universal quantum computing. However, at least one of these gates cannot be transversal for the encoded qubits¹¹. Consequently, at least one logical gate must be implemented through alternative methods to achieve universal FT computation, which often implies a substantial resource overhead¹¹.

Two well-known methods for completing a universal gate set are magic-state injection and code switching. It is possible with magic-state injection to implement a non-Clifford gate by preparing a magic resource state fault-tolerantly on a logical auxiliary qubit^[2,13] and injecting this auxiliary state onto the encoded data qubit^[14].

¹Universität Innsbruck, Institut für Experimentalphysik, Innsbruck, Austria. ²Institute for Quantum Information, RWTH Aachen University, Aachen, Germany. ³Institute for Theoretical Nanoelectronics (PGI-2), Forschungszentrum Jülich, Jülich, Germany. ⁴Present address: Alpine Quantum Technologies GmbH, Innsbruck, Austria. ⁵These authors contributed equally: Ivan Pogorelov, Friederike Butt.  e-mail: thomas.monz@uibk.ac.at

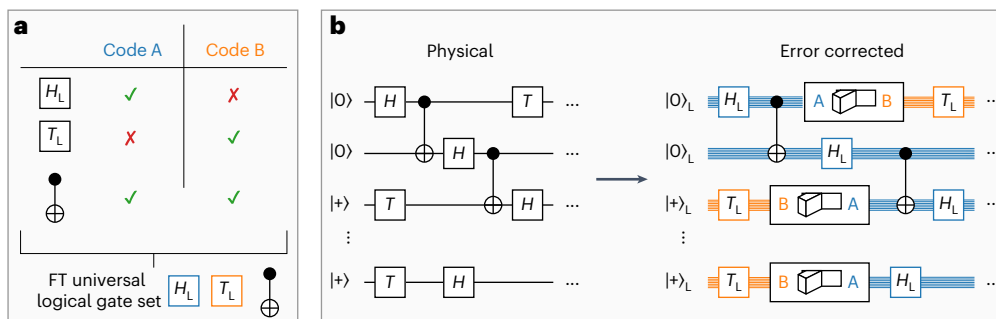


Fig. 1 | Quantum algorithms with a universal gate set. **a**, Two codes with complementary sets of FT gates in combination amount to a complete FT universal logical gate set $\{H_L, T_L, \text{CNOT}_L\}$. **b**, An algorithm running on physical qubits (left) can be run fault-tolerantly on logical qubits (right) by switching

between two codes. If, for example, the FT T_L gate is available only to code B (orange), one has to switch to this code before applying the respective gate operation.

Magic states have been prepared on superconducting architectures¹⁵ and on ion-trap quantum processors¹⁶ and a full universal gate set has recently been realized on an ion-trap quantum processor¹⁷. However, producing high-fidelity magic states poses a notable challenge and presents a large overhead¹⁸. As an alternative method, switching between two codes with complementary sets of transversal gates also enables the implementation of a full universal gate set^{19–21}, as illustrated in Fig. 1. Here, the key idea is to transfer encoded information from one encoding to another by measuring a set of operators and applying local Pauli operations. These are chosen in a way that fixes the state in the desired code space but also preserves the encoded information. An experimental demonstration of this route to fault tolerance has so far not been achieved.

In previous theoretical work, we developed FT code switching protocols using flag qubits, as introduced by refs. 12,22,23, and we found schemes that reach a level of performance competitive with magic-state injection²⁴. In this work, we present an experimental implementation of such FT code switching protocols. The protocols implemented are summarized in Supplementary Table 1. We characterized the performance of the essential building blocks for switching between the 7-qubit colour code, which encodes a single logical qubit and can correct a single error, and an error-detecting 10-qubit code²⁵ on an ion-trap quantum processor. We prepared 12 different states with the 7-qubit colour code, which cannot be obtained transversally using a single error-correcting code. We then extended these protocols to entangling logical operations and implemented minimal logical algorithms using all the gates of a universal gate set $\{H, T, \text{CNOT}\}$.

FT code switching procedure

The 7-qubit colour code encodes $k = 1$ logical qubit in $n = 7$ physical qubits and has a code distance $d = 3$, which allows the correction of any single error^{26,27}. A valid logical state is the simultaneous $+1$ eigenstate of the stabilizer generators $A_g^{(i)}$, which are shown in Fig. 2 on the left and given explicitly in ‘FT code switching between [[7, 1, 3]] and [[10, 1, 2]]’. The logical Pauli operators of this code correspond to applying Pauli X and Z operations to all seven qubits, $X_L = X^{\otimes 7}$ and $Z_L = Z^{\otimes 7}$. A logical Hadamard gate H_L can be implemented transversally by bitwise application of single-qubit Hadamard gates and, similarly, the phase gate S_L can be realized in a transversal manner by applying single-qubit S gates to all qubits. As introduced in ref. 25, the [[10, 1, 2]] code encodes a single logical qubit in 10 physical qubits and, with distance $d = 2$, can detect any single error. The logical qubit of the [[10, 1, 2]] code is defined by the stabilizer generators $B_g^{(i)}$, shown in Fig. 2 on the right and given in ‘FT code switching between [[7, 1, 3]] and [[10, 1, 2]]’. The logical Pauli operators coincide with those of the 7-qubit colour code. The X and Z stabilizer generators are not defined on the same support, meaning

that the [[10, 1, 2]] code is not self-dual and, consequently, does not have a transversal Hadamard gate. It was generated from the larger 15-qubit tetrahedral code and inherited its FT non-Clifford T gate, which can be implemented with²⁵ (subscripts indicate which qubit an operator is applied to)

$$T_L = T_1 T_2^\dagger T_3 T_4^\dagger T_5 T_6^\dagger T_7 \text{CCZ}_{8,9,10}, \quad (1)$$

which includes the controlled-controlled- Z gate on qubits 8, 9 and 10. This implementation of the logical T_L gate is not transversal anymore but FT in the sense that all possible errors resulting from a single fault are still detectable (see the circuit in Extended Data Fig. 5). The [[10, 1, 2]] code is the smallest known code that has a FT T gate²⁵.

We implemented a FT universal gate set by switching between the 7-qubit colour code [[7, 1, 3]] and the [[10, 1, 2]] code^{25–27}. We can transfer encoded information between these two codes by first measuring the stabilizers of the target code, which differ from the stabilizers of the initial code. This measurement randomly projects the logical state onto a ± 1 eigenstate of the measured stabilizers. In a second step, we force the state into the $+1$ eigenstate of the measured stabilizers without changing the logical state^{19,21,28} by applying a combination of Pauli generators. These generators directly correspond to stabilizer operators of the initial code and, therefore, do not affect the logical state.

Specifically, we measure the three Z stabilizers ($B_Z^{(4)}, B_Z^{(5)}, B_Z^{(6)}$), as shown in Fig. 2, for switching from [[7, 1, 3]] to [[10, 1, 2]]. Then, we apply a combination of the weight-4 X generators of the [[7, 1, 3]] code ($A_X^{(1)}, A_X^{(2)}, A_X^{(3)}$). For example, if the random projection onto the Z stabilizers yielded $(0, 0, 1)$, where 0 corresponds to a $+1$ eigenvalue and 1 to a -1 eigenvalue of the measured operator, we would apply $A_X^{(3)} = X_3 X_4 X_6 X_7$. $A_X^{(3)}$ overlaps at an even number of sites with $B_Z^{(4)}, B_Z^{(5)}$ and only at a single site with $B_Z^{(6)}$, and therefore, this operation fixes the state into the $+1$ eigenstate of all Z stabilizers ($B_Z^{(4)}, B_Z^{(5)}, B_Z^{(6)}$) of the 10-qubit code. For switching in the inverse direction from [[10, 1, 2]] to [[7, 1, 3]], we employ the same scheme but interchange the sets of stabilizers. We measure $(A_X^{(1)}, A_X^{(2)}, A_X^{(3)})$ and apply a combination of $(B_Z^{(4)}, B_Z^{(5)}, B_Z^{(6)})$. The lookup table with possible measurement outcomes and switching operations for both directions is summarized in Extended Data Table 1.

To achieve fault tolerance, we repeat measurements to correct for single measurement faults. We use flag qubits for stabilizer measurements to prevent faults on auxiliary qubits from propagating uncontrollably^{12,22–24,29}, and we perform further stabilizer measurements to detect potentially dangerous errors on data qubits. Whenever a potentially dangerous error is detected, the corresponding run is discarded. The full FT protocols for switching in both directions are discussed and summarized in ‘FT code switching between [[7, 1, 3]] and [[10, 1, 2]]’.

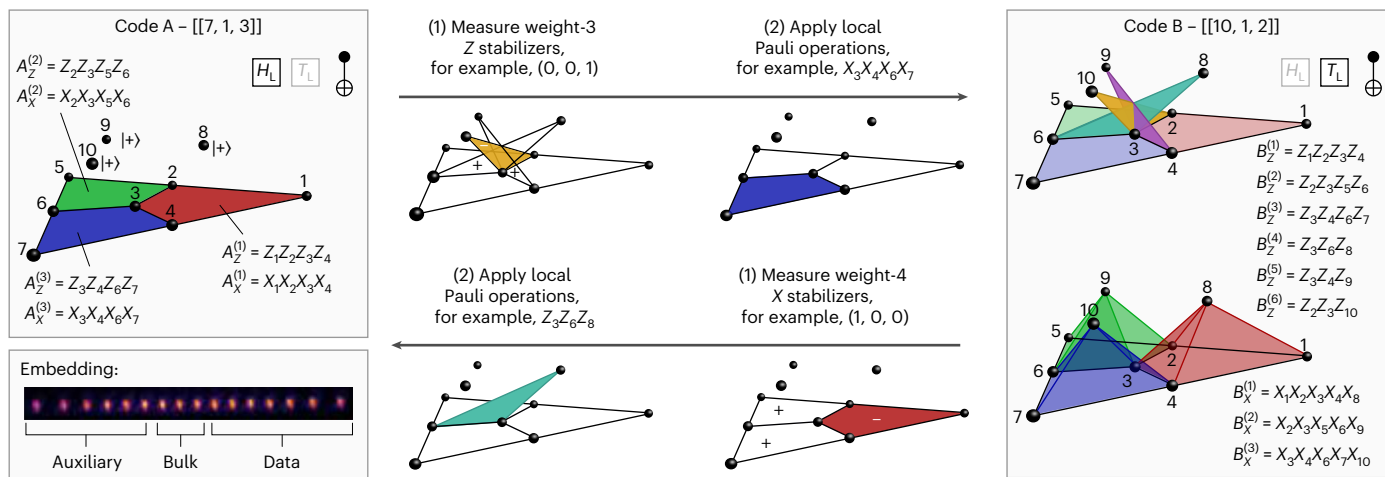


Fig. 2 | Switching between [[7, 1, 3]] and [[10, 1, 2]]. A valid code state of the [[7, 1, 3]] code (left) is a +1 eigenstate of the X and Z stabilizers $A_X^{(i)}$ and $A_Z^{(i)}$, which are defined symmetrically on the weight-4 plaquettes (red, green and blue). By contrast, the X and Z stabilizers of the [[10, 1, 2]] code (right) differ. Z stabilizers are defined on the three weight-4 plaquettes in the triangular plane (red, green and blue) and on the three weight-3 plaquettes connecting the triangular plane with the bulk qubits 8, 9 and 10 (orange, turquoise and purple). The X stabilizers of the [[10, 1, 2]] code have support on the weight-5 pyramids

(red, green and blue). To switch from the [[7, 1, 3]] code to the [[10, 1, 2]] code, we measure the three weight-3 Z stabilizers that connect the encoded [[7, 1, 3]] on qubits 1–7 with the bulk qubits 8, 9 and 10. Based on the switching syndrome obtained, a combination of the weight-4 plaquettes ($A_X^{(1)}, A_X^{(2)}, A_X^{(3)}$) is applied, which fixes the logical state in the desired code space while preserving the encoded information. The inverse switching direction is implemented analogously. First, the three weight-4 X stabilizers are measured, which is followed by the application of a combination of ($B_Z^{(4)}, B_Z^{(5)}, B_Z^{(6)}$).

Experimental set-up

The experiment was performed with a 16-ion chain of ${}^{40}\text{Ca}^+$ ions trapped in a linear Paul trap. We used an optical qubit encoded in $|0\rangle = |4^2\text{S}_{1/2}, m_J = -1/2\rangle$ and $|1\rangle = |3^2\text{D}_{5/2}, m_J = -1/2\rangle$ Zeeman sublevels. An optical addressing system with 729 nm laser light driving the qubit transition allowed us to control individual qubits. In addition, ion–ion interactions through common motional modes of the trap provided all-to-all connectivity for 2-qubit gates based on the Mølmer–Sørensen interaction³⁰. A more detailed description of the experimental set-up is given in refs. 17,31,32.

The set-up detected the ion chain using the electron shelving technique such that only a desired subset of qubits was detected while the state of the other qubits was preserved. Subsequent recooling of the ion chain and reinitialization of the detected qubits allowed us to apply high-fidelity gates after the detection procedure. The undetected qubits underwent a dynamical decoupling sequence to preserve the encoded information from decoherence during idling. We used this procedure for mid-circuit measurements of the auxiliary qubits for flag-based stabilizer read-out. A comprehensive overview of the procedure can be found in ref. 33. The error rates for the basic experimental qubit manipulation operations are given in Extended Data Table 2.

Results

We characterized each building block that is essential for implementing the universal gate set based on code switching: the initialization of [[10, 1, 2]] logical states, the logical T gate, and switching back and forth between the [[10, 1, 2]] and the [[7, 1, 3]] codes. We performed logical quantum process tomography, as specified in ‘Noise model and simulation methods’, for all building blocks and compared the results to the respective ideal process. All experimental results are accompanied by numerical simulations using a multi-parameter noise model described in ‘Noise model and simulation methods’, which used the experimental error rates given in Extended Data Table 2. The resulting logical process fidelities are shown in Fig. 3. All fidelities and acceptance rates obtained are given in Supplementary Table 2.

We found that the fidelities for the initialization in the non-FT (nFT) case were similar to those in the FT case, as the FT overhead for further verification was small and errors did not propagate in a

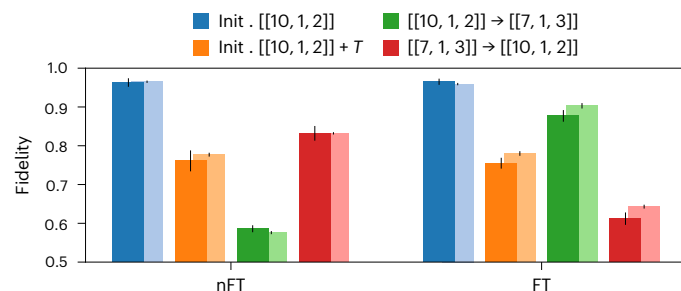


Fig. 3 | Fidelities of code switching building blocks. Logical process fidelities for the nFT protocol (left) and the FT protocol (right) for initializing the [[10, 1, 2]] logical states (blue), a logical T gate (orange), switching from [[10, 1, 2]] to [[7, 1, 3]] (green) and switching in the inverse direction (red). The values obtained in the experiment (simulation) are depicted in darker (lighter) colours. The error bars show standard deviations, determined as discussed in ‘Quantum state and process tomography’. The explicit values are summarized in Supplementary Table 2. Init., logical state initialization.

dangerous way for the nFT protocol. Only when further subsequent operations were performed on the logical state did previously correctable errors become uncorrectable, even for transversal operations, due to the different code distances for X and Z errors. For the T gate on the [[10, 1, 2]] code, we observed a similar feature, as the fidelity did not change substantially when employing the FT scheme. The FT T gate on the [[10, 1, 2]] code has another minimal error-detection block before the logical T gate, which is reflected in the decreasing acceptance rate: 81% were accepted for the nFT protocol whereas 51% were accepted for the FT version, as summarized in Supplementary Table 2. We identified the clear advantage of the FT scheme over the nFT scheme for switching from [[10, 1, 2]] to [[7, 1, 3]], as we could achieve fault tolerance with only a small increase of the 2-qubit gate count, as discussed in ‘FT code switching procedure’. However, the FT switching protocol did not provide an advantage over the nFT protocol for [[7, 1, 3]] → [[10, 1, 2]]. This was not unexpected due to the complexity of the protocol with its large circuit depth and the current error rates, which are discussed in detail in ‘FT code switching building blocks’.

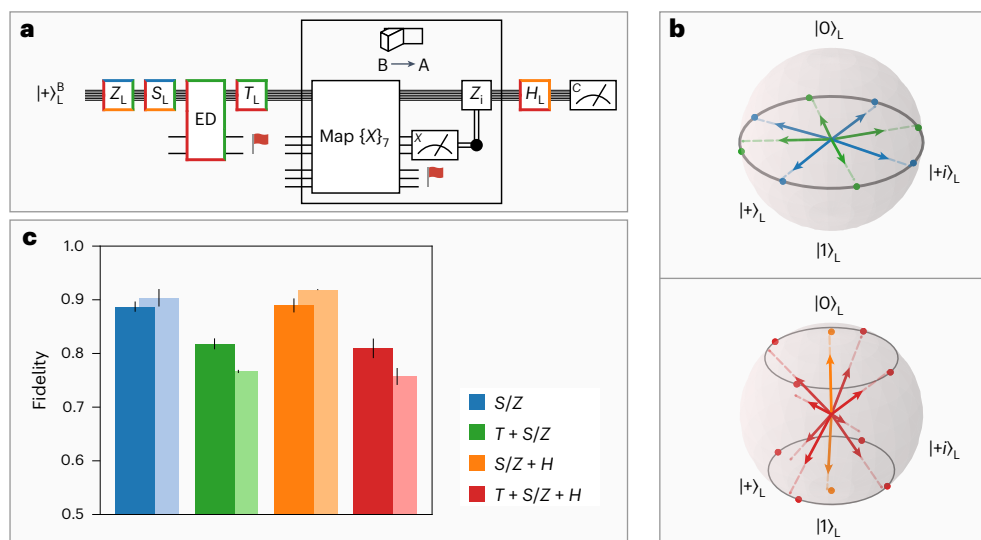


Fig. 4 | Spanning logical states on the Bloch sphere. **a**, Circuit used in the experiment to produce different logical states on the Bloch sphere. The coloured lines around gates indicate that the gate was executed to prepare the state of the respective colour. For example, the T gate was used only to produce ‘green’ or ‘red’ states. First, a logical $|+\rangle_L$ was initialized for the $[[10, 1, 2]]$ code, which was followed by operations from the gate set $\{Z, S, T\}$. The T gate was made FT by including another error-detection block before the T gate. We then switched to the $[[7, 1, 3]]$ code by measuring three weight-4 X stabilizers and applying a Z -type switching operation based on the obtained measurement outcomes. Finally, we performed $\pi/2$ rotations about the X or Y axis, which correspond to a transversal logical H gate. **b**, Bloch vectors for all states that are reachable with the different gate combinations of the protocol shown in **a**. These include the four cardinal

states on the equator of the Bloch sphere (blue) as well as those four states rotated by 45° about the Z axis (green). The north and south poles (orange) are reached by rotating about the Y axis. By applying a combination of all operations, that is the initial (non-)Clifford gates $\{S, Z, T\}$ and the final rotation, we can reach various points on the 45th parallels (grey circles) of the Bloch sphere (red). **c**, State fidelities for different logical states and for the circuit in **a**. These are averaged over groups of states with the same number of physical operations. For example, the blue bar corresponds to the fidelity averaged over the blue Bloch vectors in **b**. Experimental results are shown in darker and simulated results in lighter colours. The error bars show standard deviations, determined as discussed in ‘Quantum state and process tomography’. The values are summarized in Supplementary Table 3. ED, error-detection block. C, Clifford.

As the next step, we combined the aforementioned building blocks to prepare a variety of different states fault-tolerantly. These states are inaccessible with natively FT gate implementations in the 7-qubit colour code. The protocol is shown in Fig. 4a. Initially, $|+\rangle_L$ in $[[10, 1, 2]]$ was prepared. Then we applied the FT gates for the $[[10, 1, 2]]$ code, which includes any combinations of gates from the set $\{Z, S, T\}$. This enabled us to prepare the four cardinal states as well as four more states that require a T gate on the equator of the Bloch sphere, as shown in Fig. 4b. After switching to the 7-qubit colour code, we finally applied an H gate. This allowed us to prepare logical states on the 45th parallels of the Bloch sphere, which are not reachable with a single code with a natively FT implementation. We implemented this protocol experimentally and numerically and performed logical quantum state tomography for each state obtained. The reconstructed Bloch vectors for all prepared logical states are shown in Fig. 4b. Circuits including the non-Clifford T gate have decreased fidelity relative to purely Clifford circuits. This can be attributed to the extra 2-qubit gates required for the error-detection block before the application of the T gate and to the mid-circuit measurement, which does not have to be performed for the Clifford circuits. We identified that dephasing on idling qubits provides a major contribution to the total logical state infidelity so we took further measures to improve the fidelities of the states, prepared with the protocol in Fig. 4, which is discussed further in ‘Error budget and rotated $[[10, 1, 2]]$ ’. We could effectively increase the fidelities by up to 0.08 for Clifford states and up to 0.04 for non-Clifford states by simply reassigning the X and Z stabilizers, as shown in Extended Data Fig. 6. Such a ‘rotated’ code is more robust against Z errors and can perform better in high-dephasing environments.

We extended the demonstrated set of logical gates by entangling 2-qubit operations with the goal of exploring small logical circuits with gates from the universal gate set. We again started in the logical $|+\rangle_L$ of the $[[10, 1, 2]]$ code and could apply a FT T gate before switching to

$[[7, 1, 3]]$, as shown in Fig. 5a. For the target code, we could apply another H gate. Afterwards, a second logical qubit was prepared in the $[[7, 1, 3]]$ code in $|0\rangle_L$, and the two logical qubits were entangled with a logical CNOT. Using the full universal gate set, we prepared three entangled states with this protocol and analysed them with logical quantum state tomography, as shown in Fig. 5b,c and explicitly described in ‘Quantum state and process tomography’. Again, the experimental results and the numerically obtained fidelities agree within one standard deviation. All three logical states were entangled with $>99\%$ confidence, despite the large circuit depth and circuit complexity, which involved up to 61 2-qubit gates and two mid-circuit measurements.

Discussion

In our experimental demonstration of FT code switching, we operated all gates directly at the logical level. Code switching between error-correcting codes does not rely on the probabilistic preparation of resource states. This is important considering the observation that deterministic code execution empowered by code switching rather than a probabilistic protocol through state injection could become advantageous over probabilistic execution through state preparation and injection as overall device capabilities improve³².

We found experimentally that FT code switching schemes can notably improve fidelities in certain situations compared to their nFT counterparts. However, this advantage does not, at present, extend to protocols with a large circuit depth or many mid-circuit measurements. These primary bottlenecks in our implementation fidelity can be mitigated with technical or logical changes. In our particular implementation, we may benefit mostly from independently demonstrated technical improvements, such as extended coherence times^{34–36} and more robust composite pulse sequences during mid-circuit measurements^{37,38}. Furthermore, tailoring QEC protocols to systems with biased noise^{39–42} has the possibility of reaching higher fidelities for

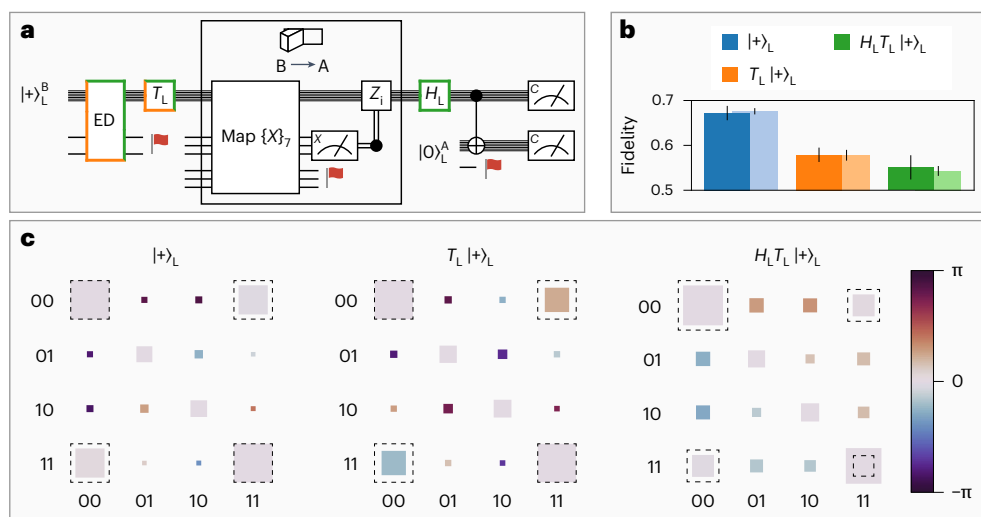


Fig. 5 | Entangling states with non-Clifford gates using code switching.

a, Protocol for preparing entangled logical qubits. A logical Bell state $\frac{1}{\sqrt{2}}(|00\rangle_L + |11\rangle_L)$ was prepared by encoding a qubit in the $[[10, 1, 2]]$ code and FT switching to $[[7, 1, 3]]$. A second qubit was then initialized in $|0\rangle_L$ in the 7-qubit colour code and coupled to the initial logical qubit by applying a transversal CNOT gate. $\frac{1}{\sqrt{2}}(|00\rangle_L + e^{i\pi/4}|11\rangle_L)$ and $\cos\frac{\pi}{8}|00\rangle_L + \sin\frac{\pi}{8}|11\rangle_L$ were prepared by including the FT T gate on the initial 10-qubit code and the $\pi/2$ rotations about the X axis on the $[[7, 1, 3]]$ code, which corresponds to a transversal logical H gate.

Coloured lines around gates indicate which gates were used to prepare the state of the corresponding colour. **b**, Fidelities for the entangled logical states that can be prepared with the different gate combinations of protocol **a**. Experiment (simulation) results are shown in darker (lighter) colours. The error bars show standard deviations, determined as discussed in ‘Quantum state and process tomography’. The values are summarized in Supplementary Table 3. **c**, Logical state tomography result for the three entangled states. The dashed black boxes indicate the ideal values corresponding to the fault-free case.

experimental set-ups with these noise characteristics. The present case with Z bias makes selecting a code like the rotated $[[10, 1, 2]]_x$, which is more resilient to Z noise, beneficial, as demonstrated by the improved performance under this exchange of stabilizers.

In the near future, code switching may be beneficial in hardware systems where the cost of mid-circuit measurements is low compared to the cost of using more auxiliary qubits for the magic-state injection. Contemporary superconducting quantum computers with limited connectivity^{43–48} and trapped-ion architectures based on quantum charge-coupled devices^{29,49–51} might fall into this category.

We considered the experimental implementation of code switching for the smallest possible instances of the respective classes of codes, namely the $[[10, 1, 2]]$ and the $[[7, 1, 3]]$ codes. Future work will include an extension from the error-detecting $[[10, 1, 2]]$ code to the deterministic error-correcting $[[15, 1, 3]]$ code, which has been explored theoretically^{21,24}, as well as longer-distance codes. An analogous CNOT protocol for the $[[15, 1, 3]] \rightarrow [[7, 1, 3]]$ switching would require 682-qubit gates and two mid-circuit measurements with 20 qubits. Code switching between error-correcting codes offers a new paradigm for implementing a deterministic set of universal gates, without the need for large-scale magic-state factories.

Online content

Any methods, additional references, Nature Portfolio reporting summaries, source data, extended data, supplementary information, acknowledgements, peer review information; details of author contributions and competing interests; and statements of data and code availability are available at <https://doi.org/10.1038/s41567-024-02727-2>.

References

- Shor, P. W. Proc. 35th Annual Symposium on Foundations of Computer Science (IEEE, 1994).
- Grover, L. K. Quantum computers can search arbitrarily large databases by a single query. *Phys. Rev. Lett.* **79**, 4709–4712 (1997).
- Preskill, J. Quantum computing in the NISQ era and beyond. *Quantum* **2**, 79 (2018).
- Gottesman, D. *Stabilizer Codes and Quantum Error Correction*. PhD thesis, California Institute of Technology (1997).
- Nielsen, M. A. & Chuang, I. L. *Quantum Computation and Quantum Information* 10th edn (Cambridge Univ. Press, 2010).
- Kitaev, A. Y. Quantum computations: algorithms and error correction. *Russ. Math. Surv.* **52**, 1191–1249 (1997).
- Aliferis, P., Gottesman, D. & Preskill, J. Quantum accuracy threshold for concatenated distance-3 codes. *Quantum Inf. Comput.* **6**, 97–165 (2006).
- Knill, E., Laflamme, R. & Zurek, W. H. Resilient quantum computation. *Science* **279**, 342–345 (1998).
- Aharanov, D. & Ben-Or, M. Fault-tolerant quantum computation with constant error rate. *SIAM J. Comput.* **38**, 1207–1282 (2008).
- Solovay, R. *Lie Groups and Quantum Circuits* (MSRI, 2000); <https://www.msri.org/workshops/189/schedules/12826>
- Eastin, B. & Knill, E. Restrictions on transversal encoded quantum gate sets. *Phys. Rev. Lett.* **102**, 110502 (2009).
- Goto, H. Minimizing resource overheads for fault-tolerant preparation of encoded states of the Steane code. *Sci. Rep.* **6**, 19578 (2016).
- Chamberland, C. & Cross, A. W. Fault-tolerant magic state preparation with flag qubits. *Quantum* **3**, 143 (2019).
- Bravyi, S. & Kitaev, A. Universal quantum computation with ideal Clifford gates and noisy ancillas. *Phys. Rev. A* **71**, 022316 (2005).
- Gupta, R. S. et al. Encoding a magic state with beyond break-even fidelity. *Nature* **625**, 259–263 (2024).
- Egan, L. et al. Fault-tolerant control of an error-corrected qubit. *Nature* **598**, 281–286 (2021).
- Postler, L. et al. Demonstration of fault-tolerant universal quantum gate operations. *Nature* **605**, 675–680 (2022).
- Gidney, C. & Fowler, A. G. Efficient magic state factories with a catalyzed $|CCZ\rangle \rightarrow |T\rangle$ transformation. *Quantum* **3**, 135 (2019).
- Kubica, A. & Beverland, M. E. Universal transversal gates with color codes: a simplified approach. *Phys. Rev. A* **91**, 032330 (2015).

20. Bombín, H. Dimensional jump in quantum error correction. *New J. Phys.* **18**, 043038 (2016).
21. Anderson, J. T., Duclos-Cianci, G. & Poulin, D. Fault-tolerant conversion between the Steane and Reed-Muller quantum codes. *Phys. Rev. Lett.* **113**, 080501 (2014).
22. Chao, R. & Reichardt, B. W. Quantum error correction with only two extra qubits. *Phys. Rev. Lett.* **121**, 050502 (2018).
23. Chamberland, C. & Beverland, M. E. Flag fault-tolerant error correction with arbitrary distance codes. *Quantum* **2**, 53 (2018).
24. Butt, F., Heußen, S., Rispler, M. & Müller, M. Fault-tolerant code switching protocols for near-term quantum processors. *PRX Quantum* **5**, 020345 (2024).
25. Vasmer, M. & Kubica, A. Morphing quantum codes. *PRX Quantum* **3**, 030319 (2022).
26. Steane, A. Multiple-particle interference and quantum error correction. *Proc. R. Soc. Lond. A* **452**, 2551–2577 (1996).
27. Bombin, H. & Martin-Delgado, M. A. Topological quantum distillation. *Phys. Rev. Lett.* **97**, 180501 (2006).
28. Poulin, D. Stabilizer formalism for operator quantum error correction. *Phys. Rev. Lett.* **95**, 230504 (2005).
29. Hilder, J. et al. Fault-tolerant parity readout on a shuttling-based trapped-ion quantum computer. *Phys. Rev. X* **12**, 011032 (2022).
30. Sørensen, A. & Mølmer, K. Entanglement and quantum computation with ions in thermal motion. *Phys. Rev. A* **62**, 022311 (2000).
31. Pogorelov, I. et al. Compact ion-trap quantum computing demonstrator. *PRX Quantum* **2**, 020343 (2021).
32. Heußen, S. et al. Strategies for a practical advantage of fault-tolerant circuit design in noisy trapped-ion quantum computers. *Phys. Rev. A* **107**, 042422 (2023).
33. Postler, L. et al. Demonstration of fault-tolerant Steane quantum error correction. *PRX Quantum* **5**, 030326 (2024).
34. Harty, T. P. et al. High-fidelity preparation, gates, memory, and readout of a trapped-ion quantum bit. *Phys. Rev. Lett.* **113**, 220501 (2014).
35. Ruster, T. et al. A long-lived Zeeman trapped-ion qubit. *Appl. Phys. B* **122**, 254 (2016).
36. Wang, P. et al. Single ion qubit with estimated coherence time exceeding one hour. *Nat. Commun.* **12**, 233 (2021).
37. Wimperis, S. Composite pulses with rectangular excitation and inversion profiles. *J. Magn. Reson.* **83**, 509–524 (1989).
38. Wimperis, S. Broadband, narrowband, and passband composite pulses for use in advanced NMR experiments. *J. Magn. Reson.* **109**, 221–231 (1994).
39. Bonilla Ataides, J. P., Tuckett, D. K., Bartlett, S. D., Flammia, S. T. & Brown, B. J. The XZZX surface code. *Nat. Commun.* **12**, 2172 (2021).
40. Xu, Q. et al. Tailored XZZX codes for biased noise. *Phys. Rev. Res.* **5**, 013035 (2023).
41. Huang, E., Pesah, A., Chubb, C. T., Vasmer, M. & Dua, A. Tailoring three-dimensional topological codes for biased noise. *PRX Quantum* **4**, 030338 (2023).
42. Pal, A. K. et al. Relaxation times do not capture logical qubit dynamics. *Quantum* **6**, 632 (2022).
43. Krinner, S. et al. Realizing repeated quantum error correction in a distance-three surface code. *Nature* **605**, 669–674 (2022).
44. Kelly, J. et al. State preservation by repetitive error detection in a superconducting quantum circuit. *Nature* **519**, 66–69 (2015).
45. Zhao, Y. et al. Realization of an error-correcting surface code with superconducting qubits. *Phys. Rev. Lett.* **129**, 030501 (2022).
46. Google Quantum AI Exponential suppression of bit or phase errors with cyclic error correction. *Nature* **595**, 383–387 (2021).
47. Satzinger, K. et al. Realizing topologically ordered states on a quantum processor. *Science* **374**, 1237–1241 (2021).
48. Takita, M., Cross, A. W., Córcoles, A. D., Chow, J. M. & Gambetta, J. M. Experimental demonstration of fault-tolerant state preparation with superconducting qubits. *Phys. Rev. Lett.* **119**, 180501 (2017).
49. Pino, J. M. et al. Demonstration of the trapped-ion quantum CCD computer architecture. *Nature* **592**, 209–213 (2021).
50. Ryan-Anderson, C. et al. Realization of real-time fault-tolerant quantum error correction. *Phys. Rev. X* **11**, 041058 (2021).
51. Wan, Y. et al. Ion transport and reordering in a 2D trap array. *Adv. Quantum Technol.* **3**, 2000028 (2020).

Publisher's note Springer Nature remains neutral with regard to jurisdictional claims in published maps and institutional affiliations.

Springer Nature or its licensor (e.g. a society or other partner) holds exclusive rights to this article under a publishing agreement with the author(s) or other rightsholder(s); author self-archiving of the accepted manuscript version of this article is solely governed by the terms of such publishing agreement and applicable law.

© The Author(s), under exclusive licence to Springer Nature Limited 2025

Methods

FT code switching between [[7, 1, 3]] and [[10, 1, 2]]

Stabilizer definitions. The stabilizer generators of the 7-qubit colour code [[7, 1, 3]] are given by (subscripts indicate which qubit an operator is applied to)

$$\begin{aligned} A_X^{(1)} &= X_1X_2X_3X_4, & A_Z^{(1)} &= Z_1Z_2Z_3Z_4, \\ A_X^{(2)} &= X_2X_3X_5X_6, & A_Z^{(2)} &= Z_2Z_3Z_5Z_6, \\ A_X^{(3)} &= X_3X_4X_6X_7, & A_Z^{(3)} &= Z_3Z_4Z_6Z_7. \end{aligned} \quad (2)$$

The logical qubit of the [[10, 1, 2]] code is defined by the stabilizer generators:

$$\begin{aligned} B_X^{(1)} &= X_1X_2X_3X_4X_8, \\ B_X^{(2)} &= X_2X_3X_5X_6X_9, \\ B_X^{(3)} &= X_3X_4X_6X_7X_{10}, \end{aligned} \quad (3)$$

and

$$\begin{aligned} B_Z^{(1)} &= Z_1Z_2Z_3Z_4, & B_Z^{(4)} &= Z_3Z_6Z_8, \\ B_Z^{(2)} &= Z_2Z_3Z_5Z_6, & B_Z^{(5)} &= Z_3Z_4Z_9, \\ B_Z^{(3)} &= Z_3Z_4Z_6Z_7, & B_Z^{(6)} &= Z_2Z_3Z_{10}. \end{aligned} \quad (4)$$

For both codes, the logical Pauli operators can be implemented by applying

$$\begin{aligned} X_L &= X_1X_2X_3X_4X_5X_6X_7, \\ Z_L &= Z_1Z_2Z_3Z_4Z_5Z_6Z_7. \end{aligned} \quad (5)$$

Switching operations. We measure stabilizer operators and apply local Pauli operations that correspond to so-called gauge operators of the subsystem code^{28,52} to switch between the 7-qubit colour code [[7, 1, 3]] and the [[10, 1, 2]] code. The lookup tables for switching in both directions are shown in Extended Data Table 1. Figure 2 exemplarily illustrates the scheme for switching between [[10, 1, 2]] and [[7, 1, 3]].

FT switching protocols. The following two algorithms summarize the protocols for FT switching between [[10, 1, 2]] and [[7, 1, 3]], which are described in ‘FT code switching procedure’. Extended Data Fig. 7 gives a graphical representation of the protocols.

Stabilizers can be measured by coupling a physical auxiliary qubit to the data qubits that belong to the operator to be measured⁵³. However, this scheme is not FT because single faults on auxiliary qubits can directly result in a logical failure. This can be avoided by using flag qubits^{12,13,22}. In addition, we also need to be able to identify errors on data qubits that invert the projective measurement with random outcomes²⁴. For example, consider code switching [[10, 1, 2]] → [[7, 1, 3]] where a Z error occurs on qubit 1. If we originally had directly (randomly) projected onto the correct target code space and measured the trivial switching syndrome (0, 0, 0), we would now measure the same one as illustrated in Fig. 2. This would cause us to apply the same gauge operator $Z_3Z_6Z_8$ as before, which in total amounts to a logical $Z_L = Z_1Z_3Z_6$ on the target Steane code. There are different strategies for detecting these dangerous errors on data qubits for each switching direction. For switching from [[7, 1, 3]] to [[10, 1, 2]], we can identify the potentially dangerous positions and perform further stabilizer measurements to check whether an error had occurred at one of these. For the inverse direction, we can detect these dangerous errors on data

qubits without extra stabilizer measurements. After switching in this direction, we measure qubits 8, 9 and 10 in the X basis and compare this outcome to their opposing stabilizer plaquette. For example, we compare the outcome of qubit 8 to the outcome of $A_X^{(1)} = X_1X_2X_3X_4$. As we started in a +1 eigenstate of the weight-5 cell, we know that pairs of these opposing operators have to agree so that, in total, they amount to 0 mod 2.

Noise model and simulation methods

We determined the expected fidelities of the implemented code switching protocols with Monte Carlo simulations. In the numerical simulations, each ideal circuit component was followed by an error E with a specified probability $p \in [0, 1]$, which is the probability of an error occurring. We included a depolarizing channel on all single-qubit and 2-qubit gates, which is defined by the error rates p_1 and p_2 with which one of the errors in the error sets E_1 and E_2 is applied. The error channel acting on state ρ is defined as

$$\begin{aligned} \mathcal{E}_1(\rho) &= (1 - p_1)\rho + \frac{p_1}{3} \sum_{i=1}^3 E_1^i \rho E_1^i, \\ \mathcal{E}_2(\rho) &= (1 - p_2)\rho + \frac{p_2}{15} \sum_{i=1}^{15} E_2^i \rho E_2^i. \end{aligned} \quad (6)$$

with the error sets $E_1 \in \{X, Y, Z\}$ for $k = 1, 2$ and 3 and $E_2 \in \{IX, XI, XX, IY, YI, YY, IZ, ZI, ZZ, XY, YX, XZ, ZX, YZ, ZY\}$ for $k = 1, \dots, 15$. Qubits were initialized and measured in the computational basis, and faults on these two operations were simulated by applying X-flips after and before the respective operation with probabilities p_{init} and p_{meas} . Furthermore, idling qubits dephase due to environmental fluctuations. We modelled this dephasing of idling qubits with the error channel

$$\mathcal{E}_{\text{idle}}(\rho) = (1 - p_{\text{idle}})\rho + p_{\text{idle}}Z\rho Z. \quad (7)$$

A Z fault was placed on each idling qubit with probability p_{idle} , which depends on the execution time t of the gate and the coherence time $T_2 \approx 50$ ms:

$$p_{\text{idle}} = \frac{1}{2} \left[1 - \exp \left(-\frac{t}{T_2} \right) \right]. \quad (8)$$

Finally, we performed mid-circuit detections. Auxiliary qubits were measured while the data qubits were kept intact, as discussed in ‘Experimental set-up’. Based on single-qubit process tomography, we estimated the error rates of X, Y and Z faults on the idling data qubits³³ and modelled the mid-circuit detection with an asymmetric depolarizing channel, which was specified by individual Pauli $p_{\text{inseq}}^{(x)}$, $p_{\text{inseq}}^{(y)}$ and $p_{\text{inseq}}^{(z)}$ error rates. All error rates and relevant gate durations are summarized in Extended Data Table 2.

We determined the state fidelity between two states ρ_1 and ρ_2 as

$$F(\rho_1, \rho_2) = \text{Tr} \left[\sqrt{\sqrt{\rho_1}\rho_2\sqrt{\rho_1}} \right]^2. \quad (9)$$

The process fidelity F_{pro} was calculated similarly with

$$F_{\text{pro}}(\mathcal{E}, \mathcal{F}) = F(\rho_{\mathcal{E}}, \rho_{\mathcal{F}}), \quad (10)$$

where F is the state fidelity and $\rho_{\mathcal{E}}, \rho_{\mathcal{F}}$ are the normalized Choi matrices for channels \mathcal{E}, \mathcal{F} , respectively. We used Qiskit’s Quantum Information package to calculate fidelities⁵⁴.

Experimental methods

Mid-circuit measurement. The mid-circuit measurement in our implementation set-up is a substantial technical source of errors with the

current parameters (Extended Data Table 2). Therefore, we aimed to construct our circuits in a way that minimizes the required number of mid-circuit detections. Stabilizers and flags mapped to auxiliary qubits are all measured in one mid-circuit measurement whenever possible, an example of which is shown in Extended Data Fig. 1. When not all the auxiliary qubits are used, we aimed to map information to the auxiliary qubits spatially far away from the data qubits to avoid optical crosstalk on data qubits. It is also beneficial to leave idle buffer qubits between auxiliary qubits to avoid crosstalk between auxiliary qubits. However, minimizing the number of mid-circuit measurements took priority. We specify the number of mid-circuit measurements for each protocol presented here in Extended Data Table 3.

Flag-bunching. FT code switching $[[10, 1, 2]] \rightarrow [[7, 1, 3]]$ includes the measurement of three stabilizers with flags, which requires six auxiliary qubits in total. Preparing the logical $|0\rangle_L$ state of $[[10, 1, 2]]$ also requires one auxiliary qubit as a flag for fault tolerance. Therefore, seven auxiliary qubits are required to map all the required stabilizers and flags if $[[10, 1, 2]] \rightarrow [[7, 1, 3]]$ code switching is done immediately after state preparation, such as when characterizing the building blocks (Fig. 3 and Supplementary Table 2). In the current experimental configuration, we are limited to no more than six auxiliary qubits in addition to 10 data qubits. Hence, we map two flags to the same auxiliary qubits to reduce the number of mid-circuit measurements. Bunching together the preparation flag and one of the stabilizer flags still preserves fault tolerance in this particular case. If there is only one error, no dangerous error can propagate such that both flags should be raised at the same time. Such flag-bunching is used only in this protocol.

Branching post-selection. FT code switching $[[7, 1, 3]] \rightarrow [[10, 1, 2]]$ requires mid-circuit decision-making to choose which set of stabilizers should be measured based on the result of the first mid-circuit measurement (Extended Data Fig. 7). The current configuration of the electronics hardware does not allow for fast communication between the camera and the control electronics, so mid-circuit decision-making within the qubit lifetime is, at present, not feasible. Thus, we assume that we know the result of a measurement and act accordingly instead of making a decision based on the result of the mid-circuit measurement. We discarded this experimental shot if during the analysis we found that our assumption about the measurement result was incorrect. This effectively decreased the acceptance rate for $[[7, 1, 3]] \rightarrow [[10, 1, 2]]$ by a factor of 2 compared to the protocol with mid-circuit decision-making.

Switching operation. Both code switching procedures require the application of a switching operation based on the outcome of a measurement of the stabilizers of the target code (Extended Data Table 1). This switching operation cannot be applied mid-circuit as the set-up does not have a mid-circuit decision-making feature. Therefore, we applied switching operations in classical processing with Pauli frame updates. This is possible if all the gates after the switching operation belong to the Clifford group, which is the case for all of our circuits.

Number of measurements. The total numbers of measurements performed for different protocols before post-selection are as follows: (1) building blocks, 30,000 shots per measurement basis for each input state for the $[[7, 1, 3]] \rightarrow [[10, 1, 2]]$ switching protocol and 12,500 shots for the other protocols, (2) Bloch sphere states, 5,000 shots per measurement basis for each prepared state, and (3) CNOT protocol, 15,000 shots per measurement basis for each configuration of the protocol.

FT code switching building blocks

Supplementary Table 1 summarizes the protocols implemented for the different logical input states that were investigated. It also summarizes

the process fidelities obtained for all code switching building blocks that we implemented experimentally and numerically.

We observed that the fidelity for nFT switching from $[[7, 1, 3]]$ to $[[10, 1, 2]]$ was higher than for FT switching. This had two main reasons. The first was that for the nFT protocol, we had already achieved very low logical error rates. In this case, only weight-3 Z stabilizers had to be measured, which meant that there were no dangerous faults on auxiliary qubits that could result in a logical error. Any error propagating from the auxiliary qubits to the data qubits was equivalent only to a weight-1 Z error and at least detectable on the target code. Furthermore, the nFT protocol requires only nine 2-qubit gates whereas at least 26 2-qubit gates are needed for the respective FT version of this protocol as well as for a mid-circuit detection, as summarized in Extended Data Table 3. This means that only a few possible single-fault positions on data qubits can cause a logical failure²⁴ in the nFT protocol. However, there is a somewhat big overhead in achieving fault tolerance with 2-qubit gates. This overhead in noisy operations in the FT protocol led to a decrease in fidelity with the current level of noise in gate operations.

For switching from $[[10, 1, 2]]$ to the $[[7, 1, 3]]$ code, the FT scheme uses two features: (1) the flag-based stabilizer measurement schemes and (2) the agreement check for opposing pairs of operators, as discussed in ‘FT code switching procedure’²⁴. The latter does not require any more qubits or measurements, as it can be done completely in classical post-processing. We estimated the contributions of these two features to the observed increase in fidelity by performing a partially FT experiment. We added the agreement check to only the nFT scheme and again determined the fidelity, as shown in Extended Data Fig. 2. We found that the agreement check contributed notably more to the infidelity than adding flag qubits for FT stabilizer measurements.

Quantum state and process tomography

The numbers given in ‘Results’ were obtained with logical quantum state and process tomography through a linear inversion using the Qiskit Experiments package⁵⁵. For each protocol, the data in Figs. 3 and 5b were collected in five experimental runs performed on different days. However, the performance differed slightly for each day. The consequent spread in the results was more substantial than the spread due to the finite number of shots taken for each protocol. Hence, to estimate errors, we performed logical quantum state and process tomography for each experimental run separately and then averaged the results. The figures show the mean and standard deviation of the fidelities. For Fig. 4c, logical quantum state tomography was performed for each state from Fig. 4b and the results were averaged over the states belonging to the same group (colour). The data from five experimental runs were joined to obtain the average density matrices shown in Fig. 5c, which were reconstructed using logical quantum state tomography. The reconstructed matrices are as follows:

$$\text{CNOT}_L(|+\rangle_L \otimes |0\rangle_L)$$

$$= \begin{pmatrix} 0.447 & -0.003 - 0.002i & -0.005 - 0.002i & 0.231 + 0.022i \\ -0.003 + 0.002i & 0.057 & 0.007 + 0.007i & 0.001 \\ -0.005 + 0.002i & 0.007 - 0.007i & 0.064 & -0.001i \\ 0.231 - 0.022i & 0.001 & 0.001i & 0.432 \end{pmatrix},$$

$$\text{CNOT}_L(T_L|+\rangle_L \otimes |0\rangle_L)$$

$$= \begin{pmatrix} 0.429 & -0.005 - 0.003i & 0.003 + 0.003i & 0.117 - 0.101i \\ -0.005 + 0.003i & 0.07 & -0.01 + 0.01i & 0.004 + 0.002i \\ 0.003 - 0.003i & -0.01 - 0.01i & 0.074 & -0.001 - 0.002i \\ 0.117 + 0.101i & 0.004 - 0.002i & -0.001 + 0.002i & 0.427 \end{pmatrix},$$

$$\text{CNOT}_L(H_L T_L |+\rangle_L \otimes |0\rangle_L)$$

$$= \begin{pmatrix} 0.477 & 0.029 - 0.035i & 0.025 - 0.035i & 0.125 - 0.009i \\ 0.029 + 0.035i & 0.07 & 0.012 - 0.006i & 0.03 - 0.018i \\ 0.025 + 0.035i & 0.012 + 0.006i & 0.081 & 0.023 - 0.013i \\ 0.125 + 0.009i & 0.03 + 0.018i & 0.023 + 0.013i & 0.373 \end{pmatrix}.$$

Further post-selection

The logical fidelity of the output state of the circuits can be further boosted without any extra measurements or operations by post-selecting for the trivial syndrome^{56,57}. The final measurement of the data qubits in every circuit yields stabilizer values for the corresponding QEC code. If all results with non-trivial stabilizer syndromes are discarded, the logical fidelity will increase whereas the acceptance rate will decrease. In doing so, a fraction of runs with error configurations of weight >1 is sorted out. The resulting logical fidelities and acceptance rates with further post-selection on trivial stabilizer syndromes for some protocols are given in Supplementary Table 3.

Error budget and rotated [[10, 1, 2]]

Individual error contributions. We performed numerical simulations of the non-Clifford CNOT protocol with a reduced error model in which we set to zero all error sources except for one so that we could estimate and compare contributions to the logical infidelity from the different individual error sources present, as shown in Extended Data Fig. 3. Note that the single contributions are not additive, as would be expected, as errors propagate and the different noise processes influence each other. Decoherence and mid-circuit measurements have a notable impact on the fidelity, which is comparable to that of 2-qubit gate errors. Although improving 2-qubit gate fidelities in a large ion chain is a complex problem, we anticipate improved coherence and mid-circuit measurement performance pending near-term hardware changes.

Impact of 2-qubit-entangling gate errors. We investigated the impact of the different noise processes by simulating the scaling of the logical infidelity of code switching as a function of the 2-qubit error rate p_2 . We considered both nFT and FT switching in both directions for three different settings of the noise parameters to determine how an improvement of the 2-qubit error rate would affect the total infidelity, as shown in Extended Data Fig. 4. With the current noise parameters, FT switching from [[10, 1, 2]] to [[7, 1, 3]] outperformed the nFT protocol, but the infidelity quickly reached a regime in which there was no qualitative change with a further improvement of p_2 . This is in stark contrast to the behaviour with magic-state injection³². However, this changed when the dephasing error rate on idling qubits p_{idle} and on the mid-circuit detections $p_{\text{mid-circ}}$ was reduced tenfold. In this case, the infidelity decreased by more than an order of magnitude, even for small values of p_2 . When switching from [[7, 1, 3]] to [[10, 1, 2]], nFT switching outperformed the FT protocol for the complete range of values considered for p_2 . This was inverted for a tenfold improvement of p_{idle} and $p_{\text{mid-circ}}$. FT switching then achieved smaller infidelities as the nFT scheme, even with the current value of p_2 . Note that these reduced values for the error rates are within reach, as extended coherence times have been demonstrated^{34–36} and composite pulse sequences have been shown to be more robust against crosstalk and laser amplitude noise^{37,38}, which can be applied in the mid-circuit measurements.

Dephasing-robust rotated encoding. It has been shown that performance can be improved with QEC protocols tailored to experimental systems with biased noise^{39–42}. Due to dephasing of idling qubits and during mid-circuit detections, the noise in our experimental set-up is strongly Z-biased. We can reduce the sensitivity to dephasing by simply interchanging the X- and Z-type stabilizers of the initial [[10, 1, 2]] code, thereby exploiting error-correcting properties that are advantageous

given strongly Z-biased noise. The [[10, 1, 2]] code, as described in 'FT code switching between [[7, 1, 3]] and [[10, 1, 2]]', can correct up to three Xerrors but can detect only at most one Zerror. This was an unfortunate combination for the experimental set-up, as decoherence of our qubits is one of the dominant error sources. However, the [[10, 1, 2]] code can be modified by exchanging the support of the X and Z stabilizers in equations (3) and (4). We refer to the initial code as [[10, 1, 2]]_Z and to the modified one as [[10, 1, 2]]_X or the rotated [[10, 1, 2]] code. The rotated code has the X and Z error-correcting properties exchanged, so that it can correct up to three Zerrors but can detect only at most one Xerror. By effectively exchanging the support of the X and Z stabilizers for the [[10, 1, 2]]_Z code, the logical T gate now becomes a rotation about the X axis instead of the Z axis and the physically executed operation includes other H gates before and after the previous T gate:

$$T_L^X = H^{\otimes 10} T_L^Z H^{\otimes 10}.$$

We used the [[10, 1, 2]]_X code to span different states on the Bloch sphere, as in Fig. 4, and compared its performance to the [[10, 1, 2]]_Z code (Extended Data Fig. 6). We initially prepared $|0\rangle_L$ with the [[10, 1, 2]]_X code and applied an X rotation to create various states in the Y-Z plane of the Bloch sphere (blue and green). Then, we switched to the [[7, 1, 3]] code by measuring the three Z stabilizers of the [[7, 1, 3]] code and applied $\pi/2$ rotations about the Y or Z axis, as these are not available transversally in the [[10, 1, 2]]_X code. In doing so, we prepared eight other states requiring non-Clifford gates (red) and two cardinal states (orange). By using this rotated [[10, 1, 2]] code, the fidelities improved on average by 0.046 for the states shown in blue and by 0.027 for the green states.

This occurred because the qubits spent less time in a decoherence-sensitive state and, during switching from [[10, 1, 2]]_Z, Z faults on data qubits could not propagate to the auxiliary qubits and corrupt the switching syndrome. Therefore, it can be beneficial to adjust the theoretically constructed codes based on a knowledge of the intrinsic error profile. However, for longer circuits with several mid-circuit measurements, as for the CNOT protocols shown in Fig. 5, the difference is less pronounced.

Data availability

The data provided in Figs. 3–5 and Extended Data Figs. 2, 3 and 6 in this article and the circuits used in the experiment are available via Zenodo at <https://doi.org/10.5281/zenodo.14179894> (ref. 58). All the measurement data can be provided by the corresponding author upon reasonable request.

References

52. Kribs, D., Laflamme, R. & Poulin, D. Unified and generalized approach to quantum error correction. *Phys. Rev. Lett.* **94**, 180501 (2005).
53. Preskill, J. in *Introduction to Quantum Computation and Information* (eds Lo, H.-K. et al.) 213–269 (World Scientific, 1998).
54. Qiskit, quantum information v0.25.2. IBM Quantum Documentation https://docs.quantum.ibm.com/api/qiskit/quantum_info (2021).
55. Kanazawa, N. et al. Qiskit Experiments: a Python package to characterize and calibrate quantum computers. *J. Open Source Softw.* **8**, 5329 (2023).
56. Huang, S., Brown, K. R. & Cetina, M. Comparing Shor and Steane error correction using the Bacon-Shor code. *Sci. Adv.* **10**, eadp2008 (2024).
57. Bluvstein, D. et al. Logical quantum processor based on reconfigurable atom arrays. *Nature* **626**, 58–65 (2024).
58. Pogorelov, I. et al. Experimental fault-tolerant code switching. Zenodo <https://doi.org/10.5281/zenodo.14179894> (2024).

Acknowledgements

We gratefully acknowledge support from the European Union's Horizon Europe research and innovation programme (Grant Agreement No. 101114305 (MILLENIUM-SGA1 EU Project) to C.D.M. and T.M. and Grant Agreement No. 101046968 (BRISQ) to P.S., M.M. and T.M.), the US Army Research Office (Grant No. W911NF-21-1-0007 to F.B., C.D.M. and T.M.), the ERC Starting Grant QCosmo (Grant No. 948893 to P.S.), the ERC Starting Grant QNets (Grant No. 804247 to M.M.), the Austrian Science Fund (FWF Grant DOI 10.55776/F71 (SFB BeyondC) to T.M.), the Austrian Research Promotion Agency (Contract No. 896213 (ITAQC) with P.S. and Contract No. 897481 (HPQC) with T.M.), which is funded by the European Union—NextGenerationEU, and the Office of the Director of National Intelligence, Intelligence Advanced Research Projects Activity (IARPA), under the Entangled Logical Qubits programme (Cooperative Agreement No. W911NF-23-2-0216 to I.P., F.B., L.P. and T.M.). This research is also part of the Munich Quantum Valley (K-8), which is supported by the Bavarian State Government with funds from the Hightech Agenda Bayern Plus (M.M. and T.M.). We further receive support from IQI GmbH and the German Ministry of Science and Education through the VDI within the project IQuAn (M.M.) and from the German Research Foundation under Germany's Excellence Strategy Cluster of Excellence Matter and Light for Quantum Computing (ML4Q; Grant No. EXC 2004/1' 390534769 to M.M.). The views and conclusions contained in this document are those of the authors and should not be interpreted as representing the official policies, either expressed or implied, of IARPA, the Army Research Office or the US Government. The US Government is authorized to reproduce and distribute reprints for government purposes notwithstanding any copyright notation herein. We acknowledge computing time provided at the NHR Center NHR4CES at RWTH Aachen University (Project No. p0020074) (F.B. and M.M.). This centre is funded by the Federal Ministry of Education

and Research and the state governments participating on the basis of the resolutions of the GWK for national high-performance computing at universities.

Author contributions

I.P. carried out the experiments. I.P., L.P. and C.D.M. contributed to the experimental set-up. I.P. and F.B. analysed the data. F.B. performed the numerical simulations, circuit analysis, characterization and theoretical modelling. I.P., F.B. and C.D.M. wrote the paper, with contributions from all authors. T.M., P.S. and M.M. supervised the project.

Competing interests

T.M. is connected to Alpine Quantum Technologies GmbH, a commercially oriented quantum computing company. The other authors declare no competing interests.

Additional information

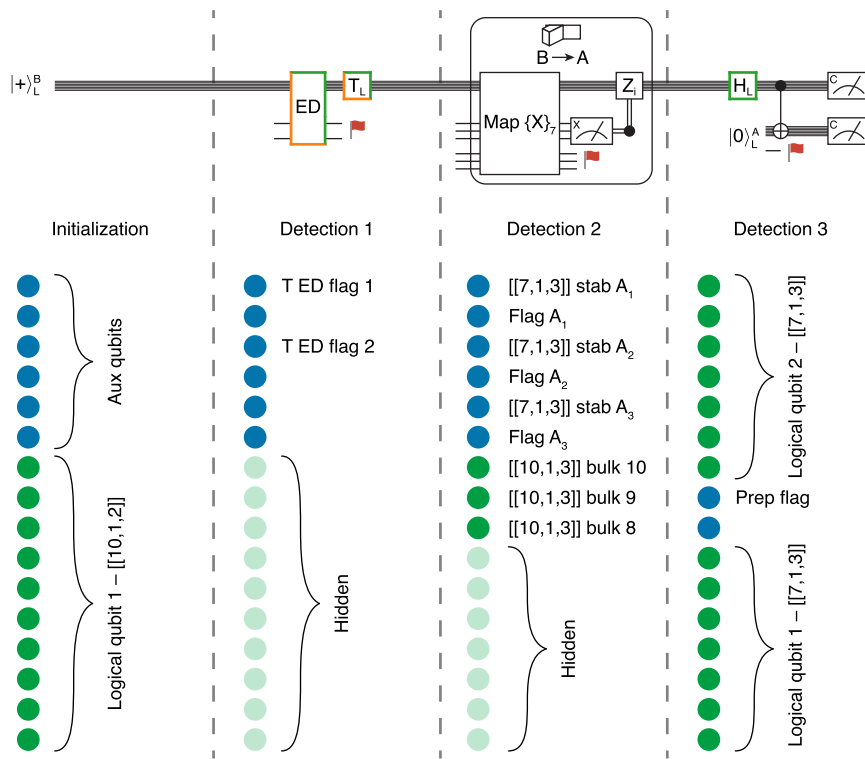
Extended data is available for this paper at
<https://doi.org/10.1038/s41567-024-02727-2>.

Supplementary information The online version contains supplementary material available at
<https://doi.org/10.1038/s41567-024-02727-2>.

Correspondence and requests for materials should be addressed to Thomas Monz.

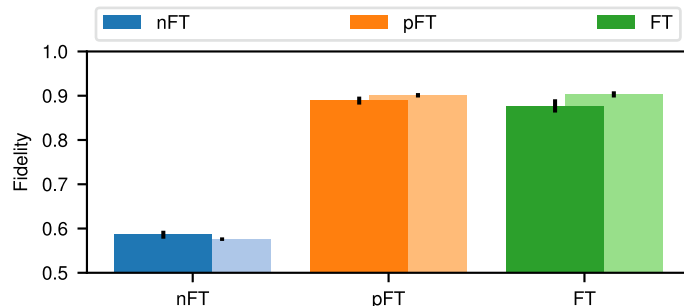
Peer review information *Nature Physics* thanks the anonymous reviewers for their contribution to the peer review of this work.

Reprints and permissions information is available at www.nature.com/reprints.



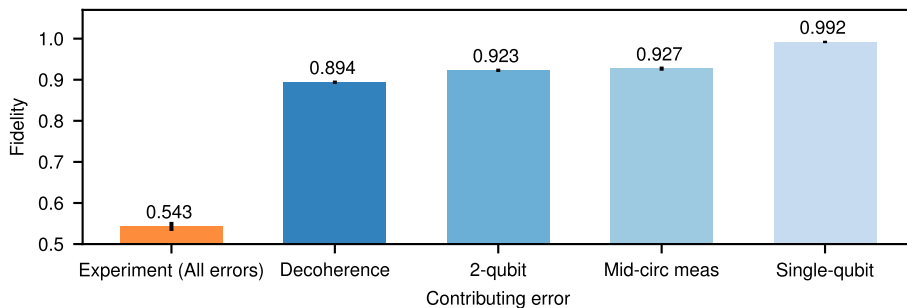
Extended Data Fig. 1 | Auxiliary qubits mapping for the entangled states generation circuit. Data qubits encoding logical states are shown in green, while auxiliary qubits used for stabilizers/flags mapping are shown in blue. There are three detections happening during the circuit, two of which are mid-circuit detections. All auxiliary qubits are detected during mid-circuit detections while

some data qubits are hidden (shown in light green). The information mapped to auxiliary qubits during each detection is shown next to qubits, no label means that the qubit is not used but still detected. After any mid-circuit detection all detected qubits are reinitialized as $|0\rangle$. All the qubits are detected during the last detection.



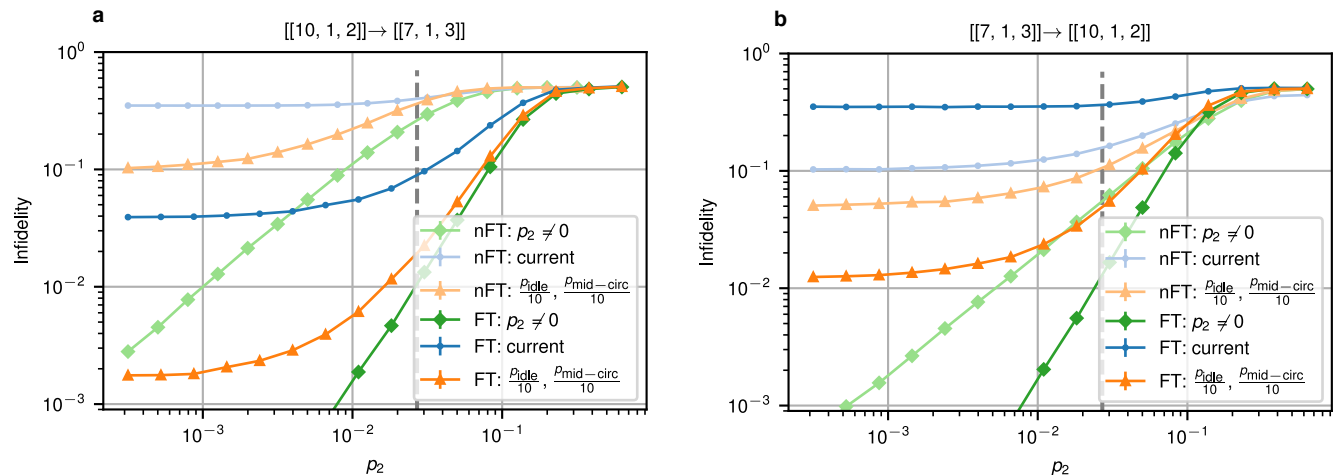
Extended Data Fig. 2 | Fidelities for partially FT code switching. Logical process fidelities of switching from the $[[10, 1, 2]]$ to the $[[7, 1, 3]]$ code, using a non-FT (blue), a partially FT (orange) and FT (green) scheme. Partially FT switching does not require additional measurements or auxiliary qubits and only includes

the agreement check of opposing pairs of operators. For FT switching, we add flag qubits for fully FT stabilizer measurements. The error bars show standard deviations, determined as discussed in ‘Quantum state and process tomography’.

**Extended Data Fig. 3 | Estimated isolated error contributions to the total infidelity.**

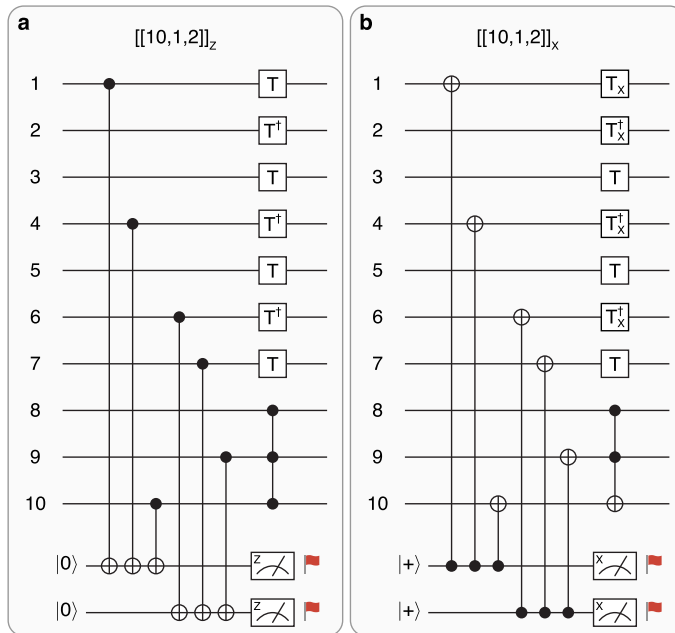
Fidelities for the non-Clifford CNOT-protocol obtained with numerical simulations. The orange column shows the fidelity for the system with realistic experimental error rates from Extended Data Tab. 2. The blue columns show the results for the reduced error model where all the errors were set to zero except for one with the corresponding fidelity indicated on top of the columns.

The non-zero error source varies between blue columns and is specified below. *Decoherence* corresponds to the dephasing of idling qubits while gates are carried out on different sets of qubits, *2-qubit* to the physical 2-qubit MS-gate error rate, *mid-circ meas* to the idling of data qubits during the measurement of auxiliary qubits and *single-qubit* to all single-qubit noise processes, including faulty initializations, measurements as well as single-qubit gates.



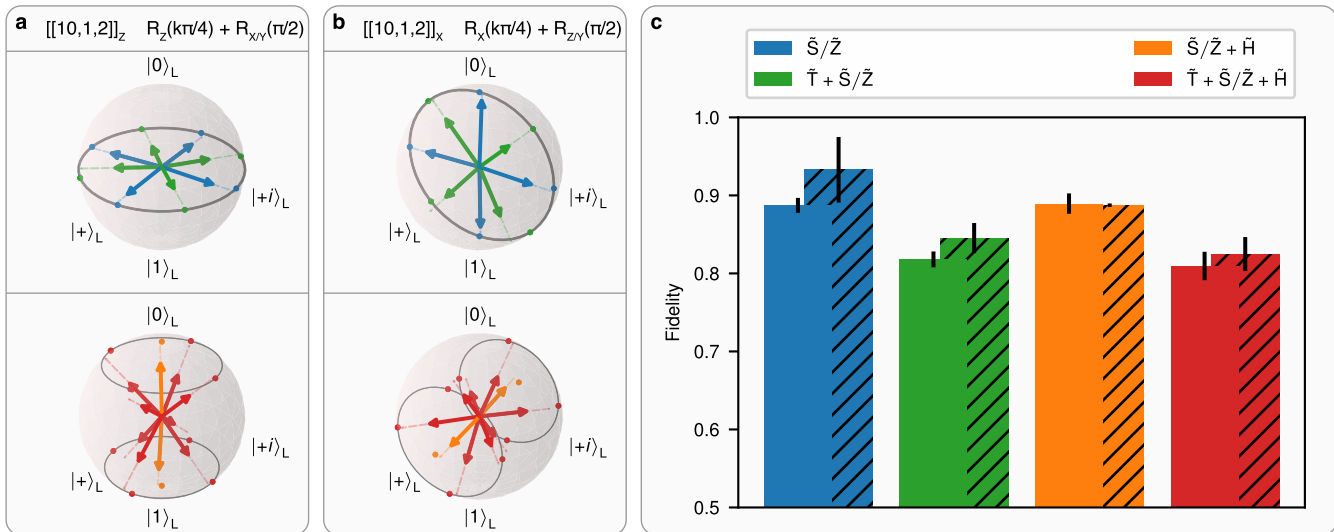
Extended Data Fig. 4 | Projected performance of code switching between $[[10, 1, 2]]$ and $[[7, 1, 3]]$. We scale the 2-qubit error rate p_2 for three different scenarios: first, for the current set of noise parameters (blue), second, for a modified set of parameters, where only the idling dephasing rate p_{idle} and the mid-circuit detection error rate $p_{\text{mid-circ}}$ are reduced by a factor of 10 (orange) and,

third, setting all error rates to 0, except for the 2-qubit error rate p_2 (green). We consider the FT and nFT switching protocols for switching (a) from $[[10, 1, 2]]$ to $[[7, 1, 3]]$ and (b) in the inverse direction. The grey dashed line corresponds to the current value of p_2 .



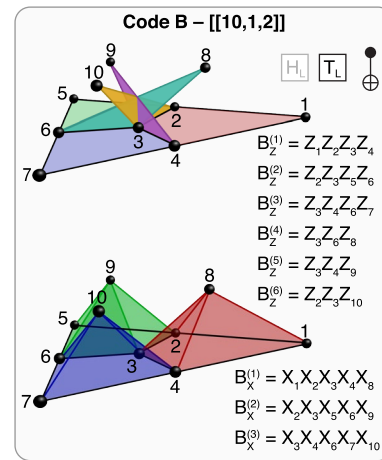
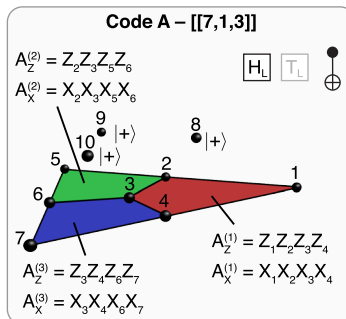
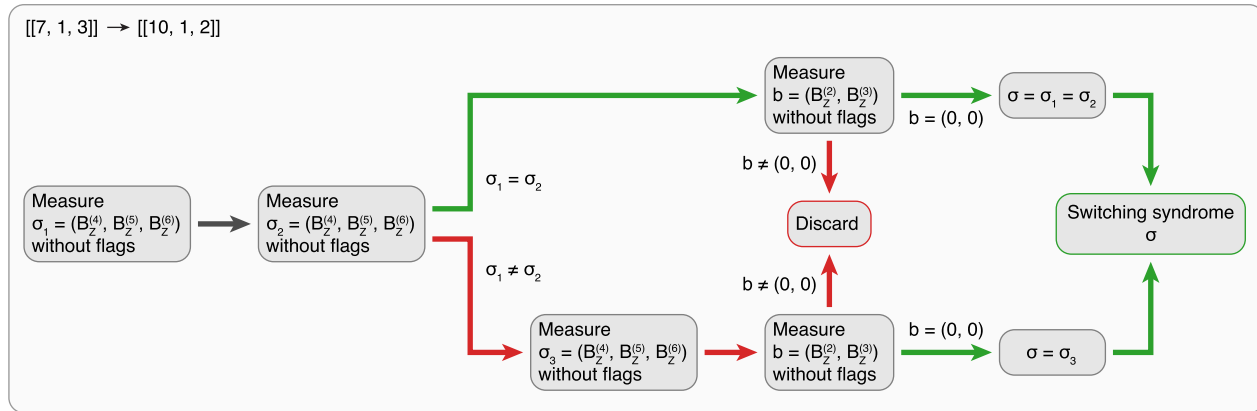
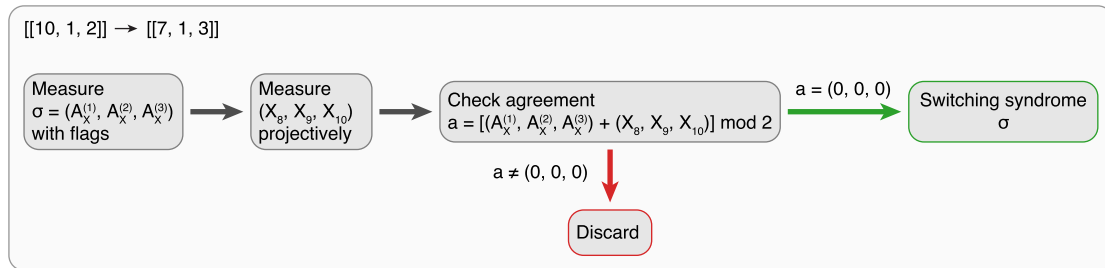
Extended Data Fig. 5 | FT logical T gate circuits. (a) The T_L^Z gate on the $[[10,1,2]]$ code can be implemented by applying single-qubit T and T^\dagger gates to qubits 1-7 and a CCZ gate to qubits 8, 9, and 10. An additional minimal error-detection block has to be performed before applying this gate that checks only for potentially

dangerous propagated X errors occurring during the initialization of the logical $|+\rangle_L$. (b) The $T_L^X = H^{\otimes 10} T_L^Z H^{\otimes 10}$ on the rotated $[[10,1,2]]$ code is implemented analogously by applying single-qubit T_x and T_x^\dagger gates on qubits 1-7 and a CCX gates to qubits 8, 9, and 10.



Extended Data Fig. 6 | Bloch states and fidelities for the rotated $[[10, 1, 2]]$ code. (a) Bloch states that were obtained for the original $[[10, 1, 2]]$ code, as shown in Fig. 4. (b) States within the Bloch sphere that were prepared with the rotated $[[10, 1, 2]]_X$ code using the analogous protocol. (c) Fidelities averaged over groups of states that require the same number of logical operations. The filled

bars correspond to the Bloch states for the original code and the hatched bars to those of the rotated version. On average, fidelities are higher for the rotated code, which is less sensitive to the dephasing. The error bars show standard deviations, determined as discussed in ‘Quantum state and process tomography’.



Extended Data Fig. 7 | Protocols for switching between [[7, 1, 3]] and [[10, 1, 2]] codes. Stabilizers of the target code are measured to obtain the switching syndrome σ . If an error happens (indicated with red arrows), the run must be discarded or additional measurements must be taken.

Extended Data Table 1 | Lookup tables for switching between [[7, 1, 3]] and [[10, 1, 2]]

Measured syndrome $(A_X^{(1)}, A_X^{(2)}, A_X^{(3)})$	Switching operation
(0, 0, 0)	—
(1, 0, 0)	$Z_3Z_6Z_8$
(0, 1, 0)	$Z_3Z_4Z_9$
(0, 0, 1)	$Z_2Z_3Z_{10}$
(1, 1, 0)	$Z_4Z_6Z_8Z_9$
(1, 0, 1)	$Z_2Z_6Z_8Z_{10}$
(0, 1, 1)	$Z_2Z_4Z_9Z_{10}$
(1, 1, 1)	$Z_2Z_3Z_4Z_6Z_8Z_9Z_{10}$

Measured syndrome $(B_Z^{(4)}, B_Z^{(5)}, B_Z^{(6)})$	Switching operation
(0, 0, 0)	—
(1, 0, 0)	$X_1X_2X_3X_4$
(0, 1, 0)	$X_2X_3X_5X_6$
(0, 0, 1)	$X_3X_4X_6X_7$
(1, 1, 0)	$X_1X_4X_5X_6$
(1, 0, 1)	$X_1X_2X_6X_7$
(0, 1, 1)	$X_2X_4X_5X_7$
(1, 1, 1)	$X_1X_3X_5X_7$

For switching from [[10, 1, 2]] to [[7, 1, 3]] (top) we measure the three X-stabilizers ($A_X^{(1)}, A_X^{(2)}, A_X^{(3)}$) and apply a Pauli Z-operation that fixes the state into the codespace of the 7-qubit color code while preserving the encoded information. For the inverse direction (bottom), we measure the three weight-3 Z-stabilizers of the [[10, 1, 2]] code ($B_Z^{(4)}, B_Z^{(5)}, B_Z^{(6)}$) and apply a suitable Pauli X operation.

Extended Data Table 2 | Depolarizing error rates and duration of operations on a trapped-ion quantum processor³³

Operation	Error rate	Duration
Two-qubit gate	$p_2 = 0.027$	322.5 μs
Single-qubit gate	$p_1 = 0.0036$	25 μs
Measurement	$p_{\text{meas}} = 0.003$	
Preparation	$p_{\text{init}} = 0.003$	
Mid-circuit detection	$p_{\text{mid-circ}}^{(x)} = 0.011$ $p_{\text{mid-circ}}^{(y)} = 0.024$ $p_{\text{mid-circ}}^{(z)} = 0.035$	
Coherence time		$T_2 = 50 \text{ ms}$

Extended Data Table 3 | Number of 2-qubit gates and mid-circuit measurements for different FT protocols

	TQ gates	Mid-circ
$ 0\rangle_L^B$	15	0
$ +\rangle_L^B$	13	0
T_L	12	0
$ \psi\rangle_L^B \rightarrow \psi\rangle_L^A$	18	0
$ \psi\rangle_L^A \rightarrow \psi\rangle_L^B$	26/35	1/2
$T_L +\rangle_L^B \rightarrow T_L +\rangle_L^A$	43	1
Clifford CNOT-protocol	49	1
non-Clifford CNOT-protocol	61	2

Code B corresponds to [[10, 1, 2]] and code A to [[7, 1, 3]]. The CNOT-protocol includes the FT initialization of $|+\rangle_L^B$, FT switching to the 7-qubit color code, the initialization of a second logical qubit $|0\rangle_L^A$ and a transversal CNOT-gate, and has the highest number of 2-qubit gates and mid-circuits measurements.